FULL PAPER

Open Access

Initial products of Akatsuki 1-μm camera

Naomoto Iwagami[1*] , Takeshi Sakanoi[2], George L. Hashimoto[3], Kenta Sawai[3], Shoko Ohtsuki[4], Seiko Takagi[5], Kazunori Uemizu[6], Munetaka Ueno[7], Shingo Kameda[8], Shin-ya Murakami[9], Masato Nakamura[9], Nobuaki Ishii[9], Takumi Abe[9], Takehiko Satoh[9], Takeshi Imamura[10], Chikako Hirose[9], Makoto Suzuki[9], Naru Hirata[11], Atsushi Yamazaki[9], Takao M. Sato[9], Manabu Yamada[12], Yukio Yamamoto[9], Tetsuya Fukuhara[8], Kazunori Ogohara[13], Hiroki Ando[14], Ko-ichiro Sugiyama[15], Hiroki Kashimura[16] and Toru Kouyama[17]

Abstract

The status and initial products of the 1-μm camera onboard the Akatsuki mission to Venus are presented. After the successful retrial of Venus' orbit insertion on Dec. 2015 (5 years after the failure in Dec. 2010), and after a long cruise under intense radiation, damage in the detector seems small and fortunately insignificant in the final quality of the images. More than 600 dayside images have been obtained since the beginning of regular operation on Apr. 2016 although nightside images are less numerous (about 150 in total at three wavelengths) due to the light scattered from the bright dayside. However, data acquisition stopped after December 07, 2016, due to malfunction of the electronics and has not been resumed since then. The 0.90-μm dayside images are of sufficient quality for the cloud-tracking procedure to retrieve wind field in the cloud region. The results appear to be similar to those reported by previous 1-μm imaging by Galileo and Venus Express. The representative altitude sampled for such dayside images is estimated to be 51–55 km. Also, the quality of the nightside 1.01-μm images is sufficient for a search for active volcanism, since interference due to cloud inhomogeneity appears to be insignificant. The quality of the 0.97-μm images may be insufficient to achieve the expected spatial resolution for the near-surface H_2O mixing ratio retrievals.

Keywords: Venus, Infrared, Dayside cloud, Nightside surface

Introduction

The Akatsuki mission to Venus, also called "Venus Climate Orbiter," was planned to investigate the Venus meteorology and to solve the long-standing riddle of the atmospheric Super-Rotation. The strategy of Akatsuki to understand the mechanism of the Super-Rotation is to combine information from five nadir-viewing cameras and a horizon-viewing radio occultation instrument, to obtain various meteorological parameters at various heights. The overview of the mission is described in Nakamura et al. (2011), and its successful revival 5 years after the failure is in Nakamura et al. (2016). The Venus orbit insertion failure occurred in 2010; however, the insertion was successful in 2015 achieving a different orbit than initially planned.

Before the Akatsuki 1-μm camera, dayside imaging of Venus to retrieve wind field in the cloud region by using the 1-μm imaging has been performed by SSI (solid-state imaging) of the Galileo spacecraft at 986 nm (Belton et al. 1991) and by VIRTIS (Visible and Infrared Thermal Imaging Spectrometer) of Venus Express at 980 nm (Hueso et al. 2012). Both of them report mostly uniform westward zonal wind and slow meridional wind in the low and middle latitudes. The magnitude of the net meridional winds in Hueso et al. (2012) is below the measurement error and discards strong Hadley cell circulation at this atmospheric altitude in contrast to results in the UV (which sample higher altitudes) where the meridional winds are stronger and the Hadley cell circulation is evident. Hueso et al. (2015) with much better statistics and analysis of the data arrived at the same conclusion. Data from the Galileo spacecraft (Belton et al. 1991) have been reanalyzed by Peralta et al. (2007) who also found slow meridional winds below the measurement error. The westward wind speeds found in the 1-μm region are

*Correspondence: iwagamina@hotmail.co.jp
[1] Tokyo 156-0044, Japan
Full list of author information is available at the end of the article

Iwagami *et al. Earth, Planets and Space* (2018) 70:6

Page 2 of 19

65–75 m/s. This is slower than the nominal Super-Rotation speed of 100 m/s usually found in the UV imaging of the cloud top at around 65–72 km (Kawabata et al. 1980; Limaye and Suomi 1981; Belton et al. 1991; Peralta et al. 2007; Sanchez-Lavega et al. 2008; Ignatiev et al. 2009; Hueso et al. 2015). Some of the above concluded that the slower wind speed comes from the lower altitude sampled by the 1-μm images than in the UV region. Such estimation may be expected from the vertical wind shear of about + 1.5 m/s/km found by the Venera and the Pioneer Venus descent probes (summarized by Schubert 1983) between the surface and the cloud top.

On the nightside, there are several known IR windows that allow radiation to penetrate the clouds in the Venus atmosphere including 1.0–1.3-, 1.7- and 2.3-μm regions (Carlson et al. 1991). The 1.0–1.3-μm window has mostly been used for investigating surface properties. Lecacheux et al. (1993) and Meadows and Crisp (1996) found many topographic signatures from ground-based imaging. There are several discussions about the relationships among emissivity, topography, gravity and the possibility of active volcanos based on infrared observational data from the Venus Express (e.g., Mueller et al. 2008; Smrekar et al. 2010; Basilevsky et al. 2012), Galileo spacecraft (Hashimoto et al. 2008) and radar data from the Magellan spacecraft (Bondarenko et al. 2010). Meadows and Crisp (1996) also retrieved H_2O abundance in the near-surface atmosphere to be 45 ppmv with this 1.0–1.3-μm window.

The 1.7- and 2.3-μm windows have mainly been used for quantification of gas abundances such as CO, H_2O and HCl (e.g., Bezard and de Bergh 2007; Tsang et al. 2008; Iwagami et al. 2008, 2010; Marcq et al. 2008; Barstow et al. 2012; Arney et al. 2014) below the cloud (not exactly at the surface). They found an average H_2O abundance of 25–35 ppmv with nearly uniform hemispherical distribution.

The strategies to fulfill the scientific goals of the Akatsuki 1-μm camera are the followings.

1. Cloud tracking on dayside images to obtain the wind field to investigate the generation mechanism of the Super-Rotation by combining information from other cameras and from radio occultation.
2. Nightside 1.01-μm imaging to discover active volcanos. If an active volcano is found and is consistently monitored, it will provide various insights into the interior of Venus as well as the origin and evolution of this next-door Earth-type planet. It will also be precious information to think about the past and future evolution of our planet Earth.
3. Quantification of the emissivity of the planetary surface and H_2O abundance in the lower atmosphere by the combination of 0.90–0.97–1.01-μm images. The

goal is to characterize the chemistry of the surface materials and the lower atmosphere to understand their current state and past evolution.

The present paper provides convenient and overall information about the Akatsuki 1-μm image data showing preliminary examples of data and analysis procedures.

The data used in this study are archived in PDS3 format. The archives have DATA_SET_IDs of VCO-V-IR1-2-EDR-V1.0, VCO-V-IR1-3-CDR-V1.0 and VCO-V-IR1-3-SEDR-V1.0. The first one includes raw data, and the second one includes calibrated data and information for calibration, and the third one includes geometry information calculated by the SPICE toolkit provided by NAIF/NASA, using the VCO SPICE kernels dataset, VCO-V-SPICE-6-V1.0. These data are available from the Akatsuki science data archive site at DARTS/JAXA, http://darts.isas.jaxa.jp/planet/project/akatsuki/. The data will also be available from the Atmospheres node and the NAIF node of the Planetary Data System of NASA, https://pds.nasa.gov.

Akatsuki 1-μm camera

The camera is described in Iwagami et al. (2011); however, some brief explanations and additional information are presented here.

The camera has a focal length of 84.2 mm and an aperture ratio of f/8 with a field of view of 12° × 12°. The detector is similar to a conventional CCD (charge-couple device) but uses a 1024 × 1024 Si CSD (charge-sweeping device)/CCD. An image has a size of about 2 MB with 14-bit resolution. The camera has a six-position filter wheel with four narrow band-pass filters, a shutter and a diffuser. One of the band-pass filters is for dayside observations, and other three are for nightside observations. The characteristics for all four channels are represented in Table 1.

Figure 1a shows dayside 0.90-μm filter transmission and an expected scattered solar spectrum with a 1-nm resolution. This channel detects the solar radiation scattered by cloud particles. This figure shows that there is little interference from gas absorption. The image may

Table 1 Characteristics of the four channels of the 1-μm camera

	0.90 day	0.90 night	0.97	1.01
Central wavelength (nm)	899.3	898.1	968.2	1008.4
FWHM (nm)	8.8	29.1	38.9	41.3
Peak transmission (%)	0.287	72.0	78.4	76.1
Typical exposure (s)	7.8	30.8	30.8	30.8
Typical S/N ratio	600	30	30	100

Iwagami *et al. Earth, Planets and Space* (2018) 70:6

Page 3 of 19

be used for the cloud-tracking procedure to find out the wind field at the cloud-bottom altitudes. The representative height is expected to be 51–55 km as will be discussed later. The dayside imaging is the most important task for the 1-μm camera.

For dayside, the camera uses a narrow filter characterized in Fig. 1a with a peak transmission of only 0.29%. Note that this low transmission is needed to image Venus dayside with the same detector used for nightside images, and that dayside high signal-to-noise ratio images can be obtained with exposures of a few seconds. The capacity of the filter to block light in other wavelengths is shown in Fig. 1b with peak transmission outside the band-pass filter in the order of 10^{-7}. The ratio of the leak signal to the nominal observed signal R_{leak} is approximated as:

$$R_{leak} = \left[10^{-7} \times 1000 \text{ nm (detector band width)} \right] / \\ 0.0029 \times 10 \text{ nm (filter band width)} = 0.0034$$

as far as the solar fluxes are in the same order. This results in a signal from the 0.90-μm band that is larger than the leak signal by a factor of 300 guarantying image quality. Actually, this is one of the most important issues for any band-pass filter; an image does not make sense if blocking is poor.

Nightside filters have a higher transmission around 75% at the ranges of interest. Figure 1c shows nightside 0.90-, 0.97- and 1.01-μm filter transmissions with expected Venus' thermal emission spectra. The spectra are for various H_2O surface abundances of 15, 30 and 60 ppmv. The 0.97- and 1.01-μm pair may be used to find out the H_2O abundance in the near-surface atmosphere. The 0.97-μm output changes by a factor of two if the H_2O mixing ratio changes from 15 to 60 ppmv (Iwagami et al. 2011). Also the pair of 0.90- and 1.01-μm radiances may give information of other surface properties such as emissivity distribution. The contribution functions for those nightside channels are found in Iwagami et al. (2011). The contribution for 1.01-μm radiance is mostly (89%) from the surface.

The standard exposure is 7.8 s for the dayside and 30.8 s for the nightside (common for all three filters). Usually, the final image to be sent to Earth is a median of three images after onboard dark-level subtraction. Since the usual data transfer rate is 16 kbps, one image of 2 MB needs 1000 s to be sent to Earth. Note that one image consists of four quadrants, which are read separately (see Fig. 2); therefore, the brightness of the four quadrants may differ slightly from one to the other. The net duration needed for one final image is 23.4 s for dayside and 92.4 s for nightside. In case of an image acquisition from a distance (Venus-center to the space-craft distance) larger than 60,000 km (54,000 km to the surface), the shift in

Fig. 1 **a** Dayside 0.90-μm filter transmission (dashed curve: revised from Iwagami et al. 2011) with an expected scattered solar spectrum (solid curve) showing little interference due to Venus atmospheric gases. The peak transmission of the filter is as small as 0.29% because of one common detector and electronics for dayside and nightside. **b** 0.90-μm dayside filter blocking ability (after BARR Co.). Blocking is effective at 300–1150 nm except in the pass band around 900 nm showing optical density (OD) of seven or more. Note that transmission = 10^{-OD}. **c** Nightside 0.90-, 0.97- and 1.01-μm filter transmissions (dashed curves: revised from Iwagami et al. 2011) with expected Venus thermal emission spectra (solid curves) with a 1-nm resolution. The three spectra are for H_2O surface abundances of 15, 30 and 60 ppmv
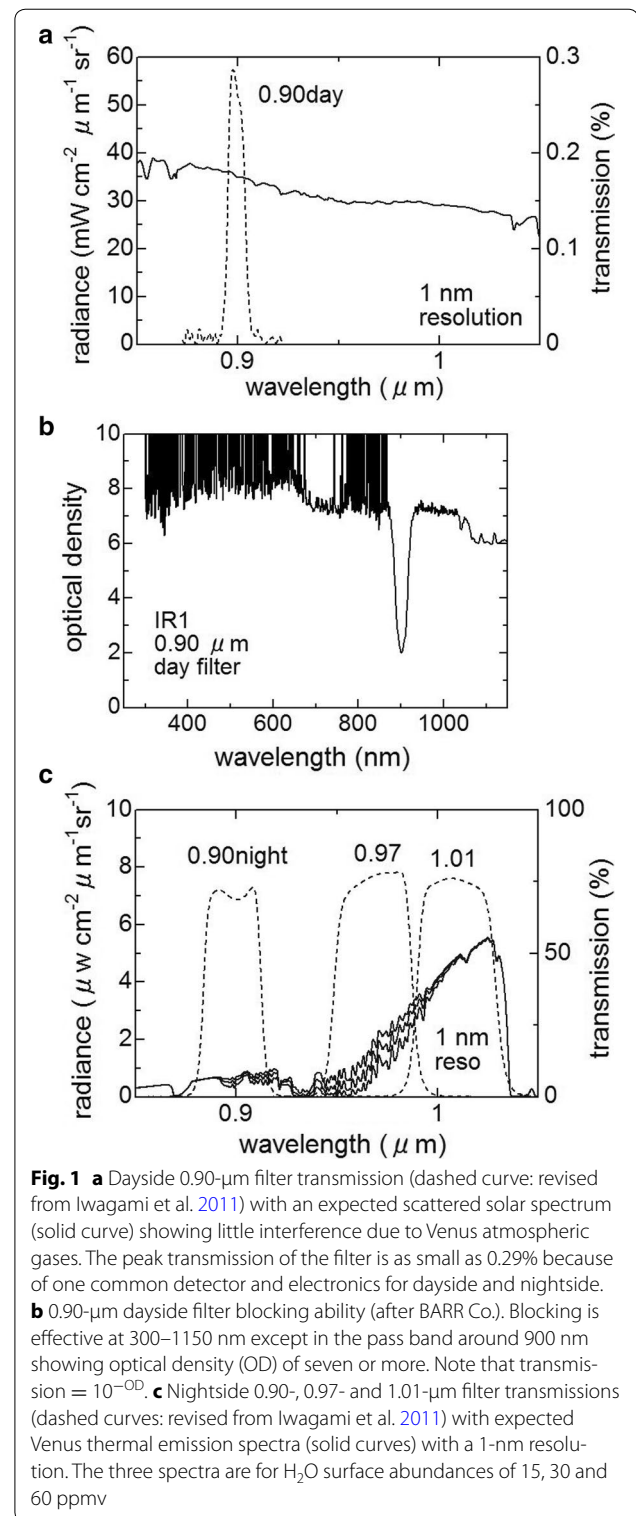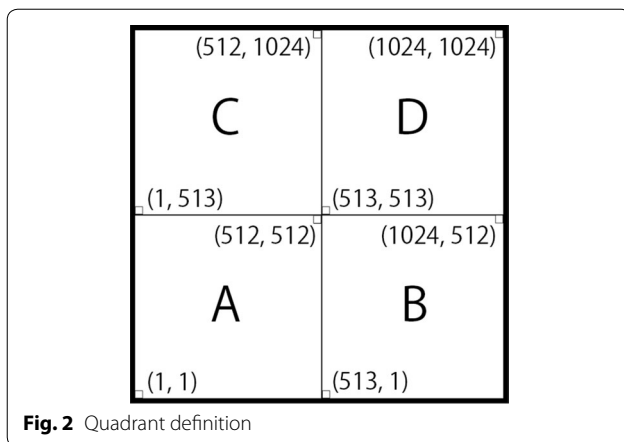
image due to Akatsuki's orbital motion will be negligible. For example, the horizontal speed is 0.10 km/s at 60,000 km; a nightside image includes a shift of 9.2 km

Iwagami *et al. Earth, Planets and Space* (2018) 70:6

Page 4 of 19

Fig. 2 Quadrant definition

which is similar to the length of one pixel size of 11.0 km at 60,000 km. When the distance is less than 60,000 km, we should be careful against a shift during exposures.

The 5-year cruise on space from the failure in orbit insertion in 2010 and the successful Venus orbit insertion in 2015 could have degraded the quality of the camera causing instrumental problems like a greater number of dead pixels. Fortunately, such degradation has been found to be minimal and well-contrasted images were obtained with the instrument. The reason for such healthy survival may be due to extremely quiet solar activity in the last 5 years. Although many dark spots have been found in

recent images by deep inspection, fortunately, they may be removed by the flattening procedure. Such dark spots may be noticed in the flat image (e.g., Figs. 9, 10) as several negative spikes.

An inflight alignment check (direction of the line of sight, rotation angle of the field of view and actual focal length) has been performed three times: on October 08, 2010, February 24, 2016, and September 09, 2016, by using six stars of the Sagittarius constellation (SAO star catalog, J2000 epoch, see Table 2). The results are compared in Table 3. In this procedure, the observed star positions are fitted to the expected star positions to find out the actual direction (C_x, C_y), rotation angle (A_{rot}) and size of the field of view (determined from R_f) by adjusting these four (C_x, C_y, A_{rot} and R_f) parameters. By minimizing the RMS (root-mean-square) distance between the observed and expected star positions, the best set of parameters is selected. The most significant fact found in Table 3 is that the line of sight (C_x, C_y) depends considerably on the spacecraft overall direction indicated by $\pm Y$ (northward or southward). For example, southward Y direction as in Feb. and Sep. of 2016 results in the line of sight at around (3E, 10S) where unit is in pixel = 0.012°; this means that the actual line of sight was found at a little different direction from the expected direction by 0.04° eastward and 0.12° southward. However, northward Y direction as in Oct. 2010 results in at around (4W, 3S). The difference is as large as 10 pixels (0.12°). The cause

Table 2 Sagittarius stars for alignment check and radiometric calibration

Star	Spectral type	m_v (mag)	T_e (K)	$F_{0.90}$	$F_{0.97}$	$F_{1.01}$
ε Sgr	B9.5 III	1.85	9960	180.4	143.7	126.8
λ Sgr	K1 + IIIb	2.82	4770	199.4	176.4	164.0
δ Sgr	K3 IIIa	2.67	4192	304.4	277.7	262.2
τ Sgr	K1 + IIIb	3.31	4459	146.5	131.6	123.3
σ Sgr	B2.5 V	2.07	20370	100.4	76.8	66.4
ζ Sgr	A2III + A4 IV	2.59	8799	102.4	82.5	73.2

m_v is visual magnitude; T_e is effective temperature in K; $F_{0.90}$, $F_{0.97}$ and $F_{1.01}$ are energy fluxes at 0.9, 0.97 and 1.01 μm, respectively, in units of 10^{-12} mW/cm²/μm

Table 3 Alignment check by stars on three days

Parameter* Unit	C_x Pixel**	C_y Pixel	A_{rot} Degree	R_f %	Res Pixel	+ Y
Initial guess	0	0	0	100		
October 08, 2010	3.7W ± 2.8	3.4S ± 2.8	0.260cw ± 0.154	99.30 ± 0.27	2.81	North
February 24, 2016	3.0E ± 3.0	10.2S ± 3.0	0.250cw ± 0.152	99.30 ± 0.29	2.99	South
September 09, 2016	3.7E ± 3.1	10.8S ± 3.1	0.264cw ± 0.150	99.25 ± 0.30	3.15	South

C_x and C_y are the center of the field of view (in unit of pixel); A_{rot} is field rotation angle (degree); R_f is focal length ratio (%); Res is fitting residual (pixel); and + Y is spacecraft direction, where 1 pixel = 0.0117°. "Initial guess" means the expected parameter value for exact camera setting

*Center of the field of view (C_x, C_y), field rotation angle (A_{rot}), focal length ratio (R_f), fitting residual (Res) and spacecraft direction (+ Y)

**1 pixel = 0.0117°

Iwagami *et al. Earth, Planets and Space* (2018) 70:6

Page 5 of 19

of such difference is not known, but one possibility may be the thermal deformation of the spacecraft body. Even after a slight attitude change before an observation, drift in the line of sight is sometimes noticed. For example, the five star images on September 09, 2016, taken every 2 h show a drift of three pixels between the 1st and 2nd images although the attitude data show a drift of less than one pixel. On the other hand, the field rotation angle (A_{rot}) and the focal length ratio (R_f) are found to be stable; they seem to be free from the thermal deformation. Because the size of the star in the image is approximately 1.5 pixels, the fitting residual (Res) is expected to be similar in amplitude; however, actual residuals found are as large as 3 pixels. Such excess residual may be due to attitude drift of the spacecraft. The proper motion of stars may be negligible because they are in the order of 0.0001°/year. Such unwanted drift in the line of sight is overcome by the use of limb-fitting technique (Ogohara et al. 2012) to find out the accurate direction of the line of sight.

Data acquisition

After the successful insertion on December 07, 2015, and the start of regular data acquisition in Apr. 2016, dayside 0.90-μm images were obtained regularly showing good contrast, but all nightside 0.90-, 0.97- and 1.01-μm images present signal contamination from the dayside, and their acquisition requires specific planning pushing the dayside out of the field of view to avoid electric charge overflowed from the bright dayside part of the image into the nightside. This kind of observation has been performed regularly after July 21, 2016. However, such operation causes another kind of contamination. It causes a bias superposed on the nightside image; such bias seems to be due to instrumental internal reflections of the dayside image.

The number of usable images is shown in Fig. 3 for Dec. 2015–Dec. 2016. The apparent 10-day periodicity is due to Akatsuki's orbital motion with a period of ten Earth-days. Nightside image acquisitions are concentrated at around periapsis. The angular size of Venus in images acquired from large distances in the Akatsuki orbit is too small to successfully separate the dayside from the nightside and results in contamination in the nightside data. The dayside image acquisition was especially successful in Jun. to Dec. consisting of every 1- or 2-h acquisition continuing several hours; the cloud tracking on such days is expected to work well.

Unfortunately, data acquisition has been stopped since December 07, 2016, due to malfunction of the electronics and has not been resumed since then.

Image corrections and calibration

An example of the image processing flow is shown in Fig. 4a, b. Figure 4a shows a Level 1 image (a raw image before correction). Figure 4b shows a Level 2 image (a cleaned image after the correction of smear-like noise and the flattening procedure represented with absolute
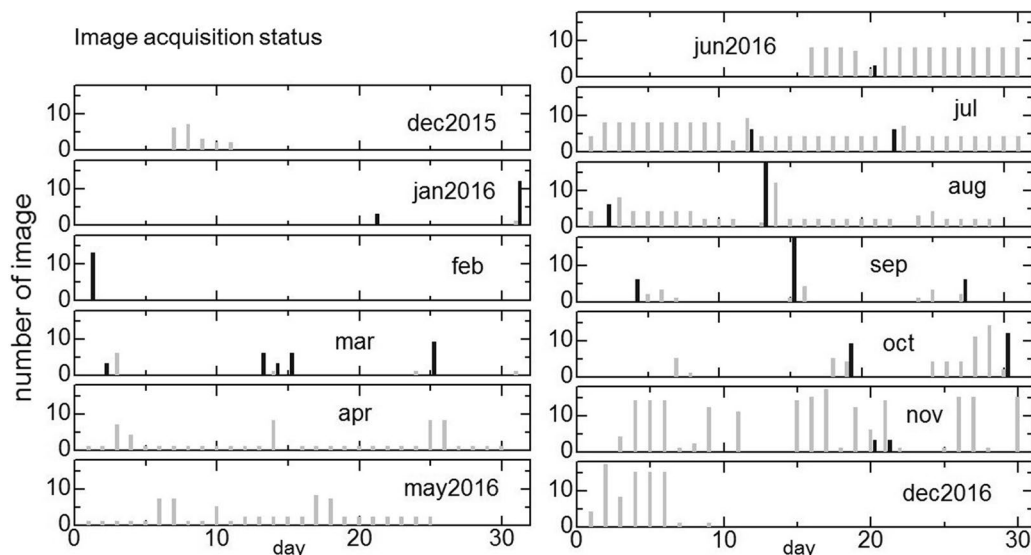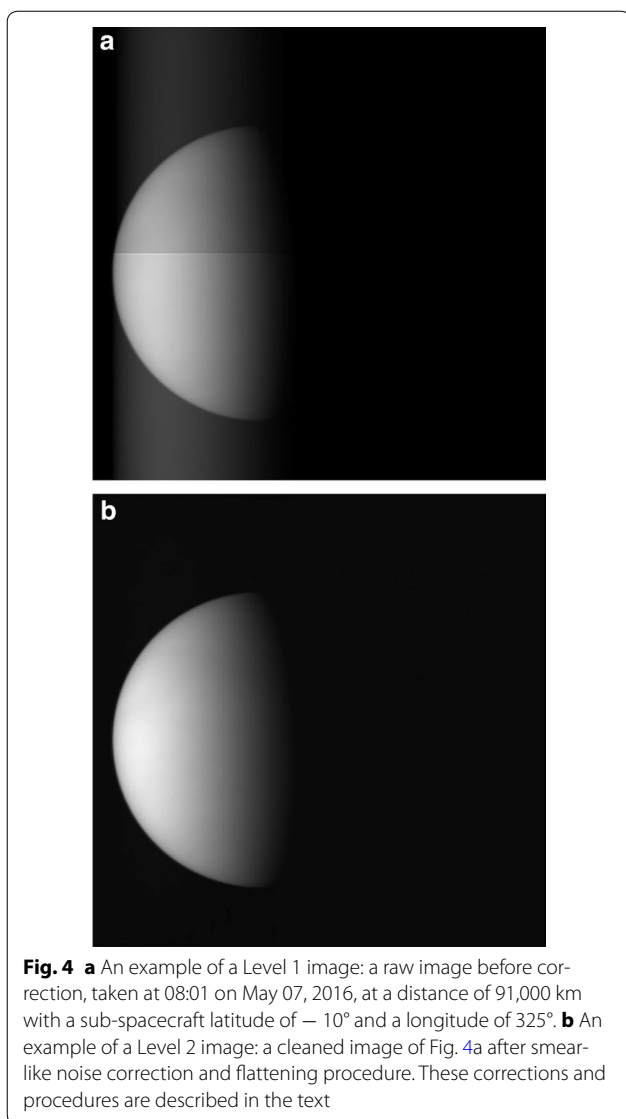

Fig. 3 Image acquisition status for Dec. 2015–Dec. 2016. Each box represents 1 month. The vertical axis is for the number of available images, and the horizontal for the day in a month. Dayside is shown by gray and nightside by black vertical bars. A set of three nightside images are taken nearly simultaneously, and the black bar indicates total number of nightside images, so that one-third of the black bars belongs to one wavelength. The 10-day periodicity seen is due to Akatsuki's orbital motion, and nightside images are concentrated around periapsis

Iwagami *et al. Earth, Planets and Space* (2018) 70:6

Page 6 of 19

Fig. 4 a An example of a Level 1 image: a raw image before correction, taken at 08:01 on May 07, 2016, at a distance of 91,000 km with a sub-spacecraft latitude of − 10° and a longitude of 325°. **b** An example of a Level 2 image: a cleaned image of Fig. 4a after smear-like noise correction and flattening procedure. These corrections and procedures are described in the text

physical values). These corrections are described in detail in the following.

Smear noise correction

The Level 1 image in Fig. 4a shows an unwanted noise similar to so-called smear noise which is believed to be due to unwanted exposure during charge transfer. In the figure, this smear-like noise is recognized as non-dark sky on the left side extending vertically. At the first stage of designing the camera, such smear-like noise should not appear because of CSD/CCD (not CCD/CCD) configuration; however, it did appear. Fortunately, elimination of such smear-like noise is not so difficult because the approximate solution is already seen in the surrounding sky. The correction is done by subtracting the radiance level seen in the surrounding sky so that the sky

becomes dark. The performance of such an operation is also demonstrated in Figs. 5, 6, 7 and 8. Since the surrounding sky in Fig. 4b (also in Figs. 6 and 8) appears to be dark, the present correction seems to work well. Also the difference in brightness seen between the upper and lower quadrants on the disk disappeared after the correction. However, the sky portion shows a little slope as in the case of Fig. 6 indicating imperfection of the present method. The procedure for the smear noise correction is explained in Appendix A.
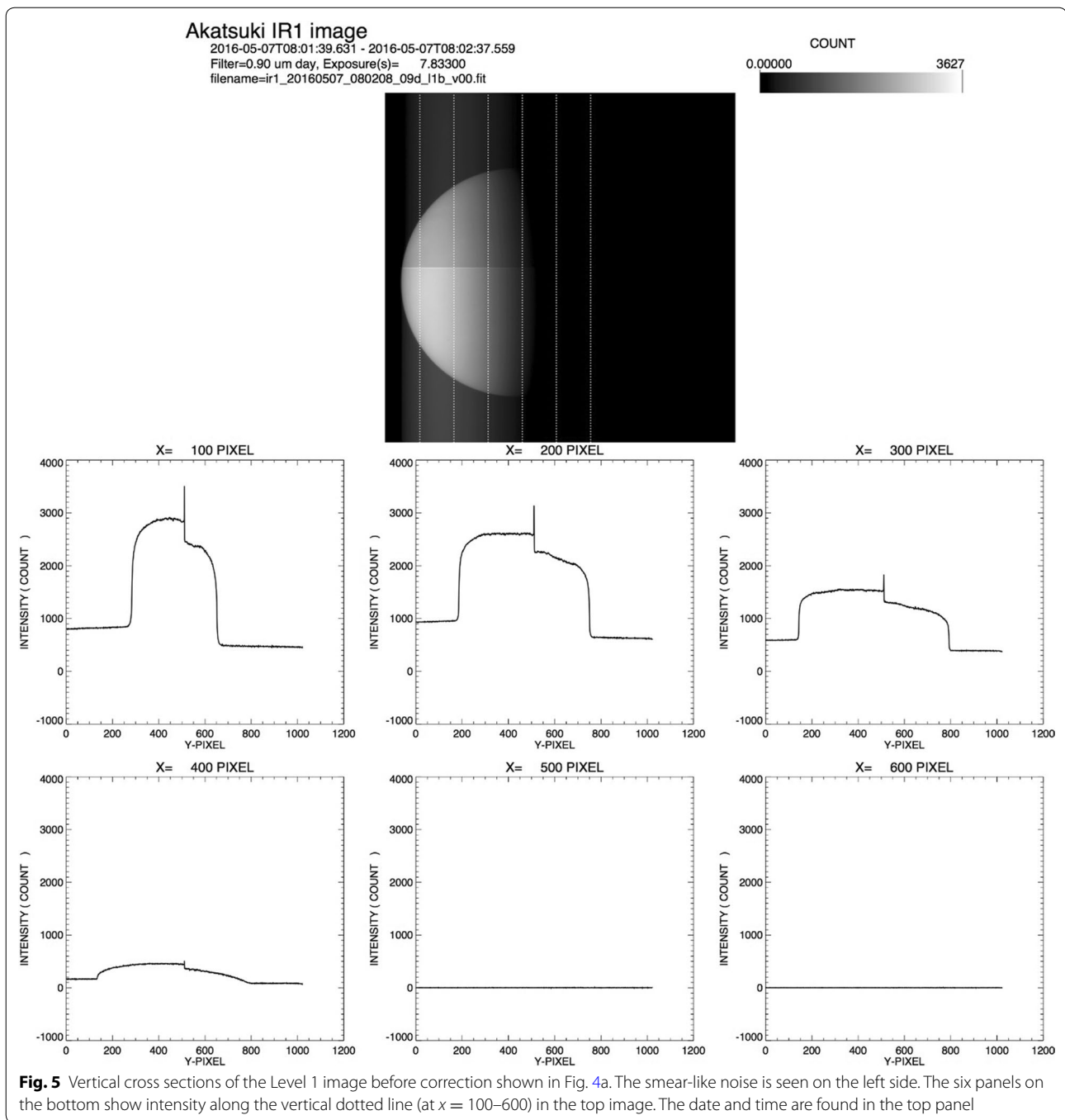
Flat-field correction

For the flat-field correction, an average of four large dayside images after smear correction taken at distances (Venus' center to the spacecraft distance) of 12,000–19,000 km is used (see Figs. 9, 10). At this distance, the disk of Venus fills the entire instrumental field of view. In this case, the Venus disk image shifts several tens of pixels during the exposure partly erasing inhomogeneity on the disk. The shift is calculated in the following way: One pixel corresponds to 1.2 km on the surface at a distance of 12,000 km (6000 km to the surface). Then, the shift during an exposure is 3.5 km/s (horizontal speed at 12,000 km) $\times$ 23 s = 81 km (67 pixels). A similar calculation for 19,000 km distance (horizontal speed of 1.8 km/s and 2.6 km/pixel) gives a shift of 41 km (16 pixels). Those shifts are effective to erase small structures of a few 10 km. Such a large dayside flat is suitable for the dayside images because of the same filter (0.90-μm filter with a width of 0.01 μm); this flat is also used for nightside images. The flat measured with the diffuser is not used because the above flat works better. However, the four images used for the average are far from identical. The variation is about 25% at maximum. The sensitivity variation within several pixels can be corrected by this method, but sensitivity variation in the several tens to hundreds pixels is possibly incorrect. In Figs. 9, 10, cross sections of the flat field are shown.

In Fig. 4a, a bright horizontal line is seen at the 513th line (brighter than the 514th line by about 20%) of the image. The cause of such a brightening is unknown, and it did not appear during the ground-based test operations. However, it is approximately corrected by the flattening procedure, fortunately, as shown in Fig. 4b. After all of this processing, the dayside images have a noise level of 0.3% which is suitable for the cloud-tracking procedure; this is demonstrated by the cloud-tracking tests in a latter section.

Quadrant brightness adjustment

Even after flat-field correction, discontinuity at the boundaries of the four quadrants (or regions) of the detector area (see Fig. 2) can be seen in several images
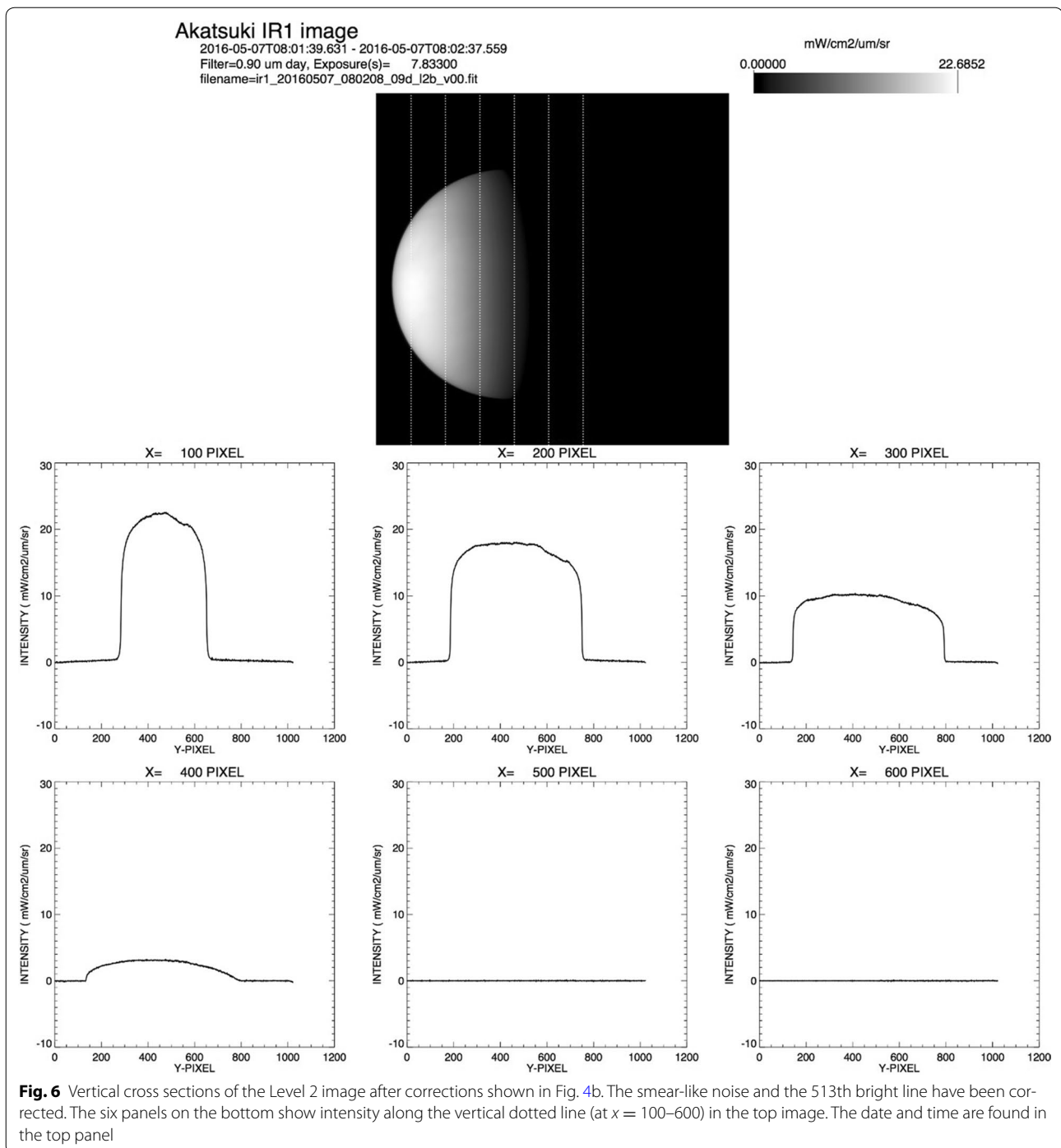
Iwagami *et al. Earth, Planets and Space* (2018) 70:6

Page 7 of 19

Fig. 5 Vertical cross sections of the Level 1 image before correction shown in Fig. 4a. The smear-like noise is seen on the left side. The six panels on the bottom show intensity along the vertical dotted line (at $x = 100$–600) in the top image. The date and time are found in the top panel

where definitions of the regions A–D (in terms of pixel numbers) are the following: A [1:512, 1:512], B [513:1024, 1:512], C [1:512, 513:1024] and D [513:1024, 513:1024]. This boundary discontinuity may be caused by a slight difference in the gain among the four readout detectors and could also contain secondary effects from incomplete reduction of the smear noise. A relative sensitivity correction for each of the four regions should be done to reduce the discontinuity at the boundaries. The correction coefficient of A–B boundary, R_{AB}, is expressed as

$$R_{AB} = (2 * S(512) - S(511))/S(513),$$

where

$$S(i) = \sum_{j=1}^{512} s(i, j).$$

Iwagami *et al. Earth, Planets and Space* (2018) 70:6

Page 8 of 19

Fig. 6 Vertical cross sections of the Level 2 image after corrections shown in Fig. 4b. The smear-like noise and the 513th bright line have been corrected. The six panels on the bottom show intensity along the vertical dotted line (at $x = 100$–600) in the top image. The date and time are found in the top panel

When R_{AB} is less than 0.5 or more than 2.0, which frequently occurs when the disk of Venus is not on the boundary, we set $R_{AB} = 1$. R_{CD}, R_{AC} and R_{BD} are estimated in the same way. If the center of Venus is in A or B region, we set R' (the correction coefficient of top (AB)–bottom (CD) boundary) $= R_{AC}$, and if it is in C or D region, we set $R' = R_{BD}$. The signals in B, C and D regions were multiplied by R_{AB}, R' and $R'R_{CD}$, respectively.

Radiometric calibration

Radiometric calibration was performed using the images of six stars of the Sagittarius constellation (see Table 2) obtained in Feb. and Sep. in 2016. We estimated the irradiance at the wavelengths of 0.90, 0.97 and 1.01 μm from the visual magnitudes and the temperatures with blackbody assumption and calculated the sensitivity coefficients in μW/cm²/μm/(ADU/s) where ADU is "analogue

Iwagami *et al. Earth, Planets and Space* (2018) 70:6

Page 9 of 19

Fig. 7 Horizontal cross section of the Level 1 image before correction shown in Fig. 4a. The six panels on the bottom show intensity along the horizontal dotted line (at y = 100–600) in the top image. The date and time are found in the top panel
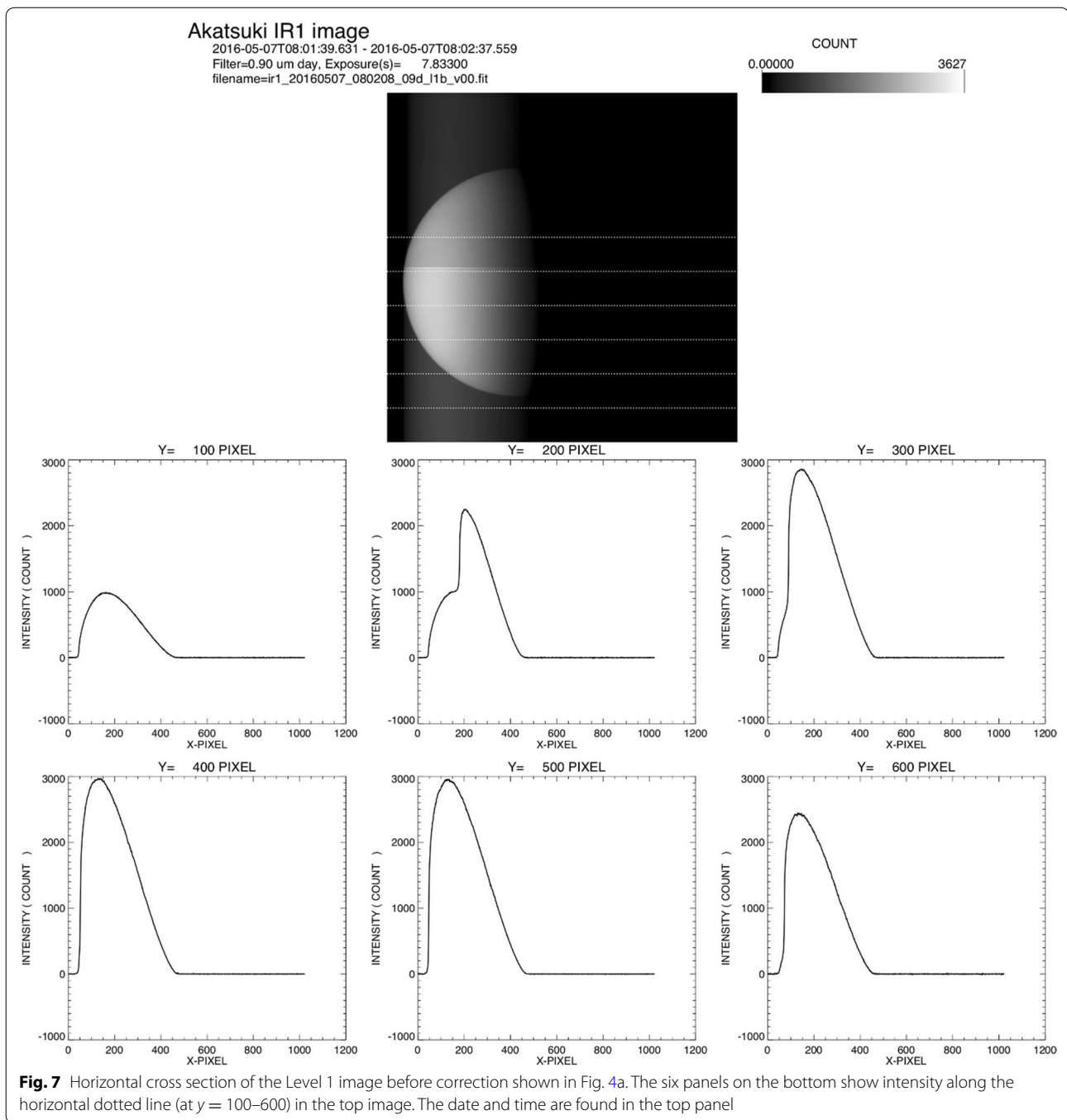
to digital conversion unit." The calculation is based on visual magnitude (defined at 550 nm) and spectral type of the stars (SAO star catalog). Effective temperature T_e is estimated from the spectrum type (Strand 1963). The star flux at 0.90-μm F_{090} is calculated as

$$F_{090} = F_{055} B(T_e, 0.90) \big/ B(T_e, 0.55)$$

with

$$F_{055} = F_{055,0\mathrm{mag}} \times 10^{-0.4\mathrm{mv}},$$

where F_{055} is the flux at 0.55 μm calculated from visual magnitude; $B(T_e, 0.90)$ and $B(T_e, 0.55)$ are the black-body function at 0.90 and 0.55 μm, respectively; $F_{055,0\mathrm{mag}} = 3.64 \times 10^{-12}$ W/cm²/μm is the flux of a zero visual magnitude star; and m_v is visual magnitude.

Iwagami *et al. Earth, Planets and Space* (2018) 70:6

Page 10 of 19

Fig. 8 Horizontal cross section of the Level 2 image after correction shown in Fig. 4b. The six panels on the bottom show intensity along the horizontal dotted line (at y = 100–600) in the top image. The date and time are found in the top panel
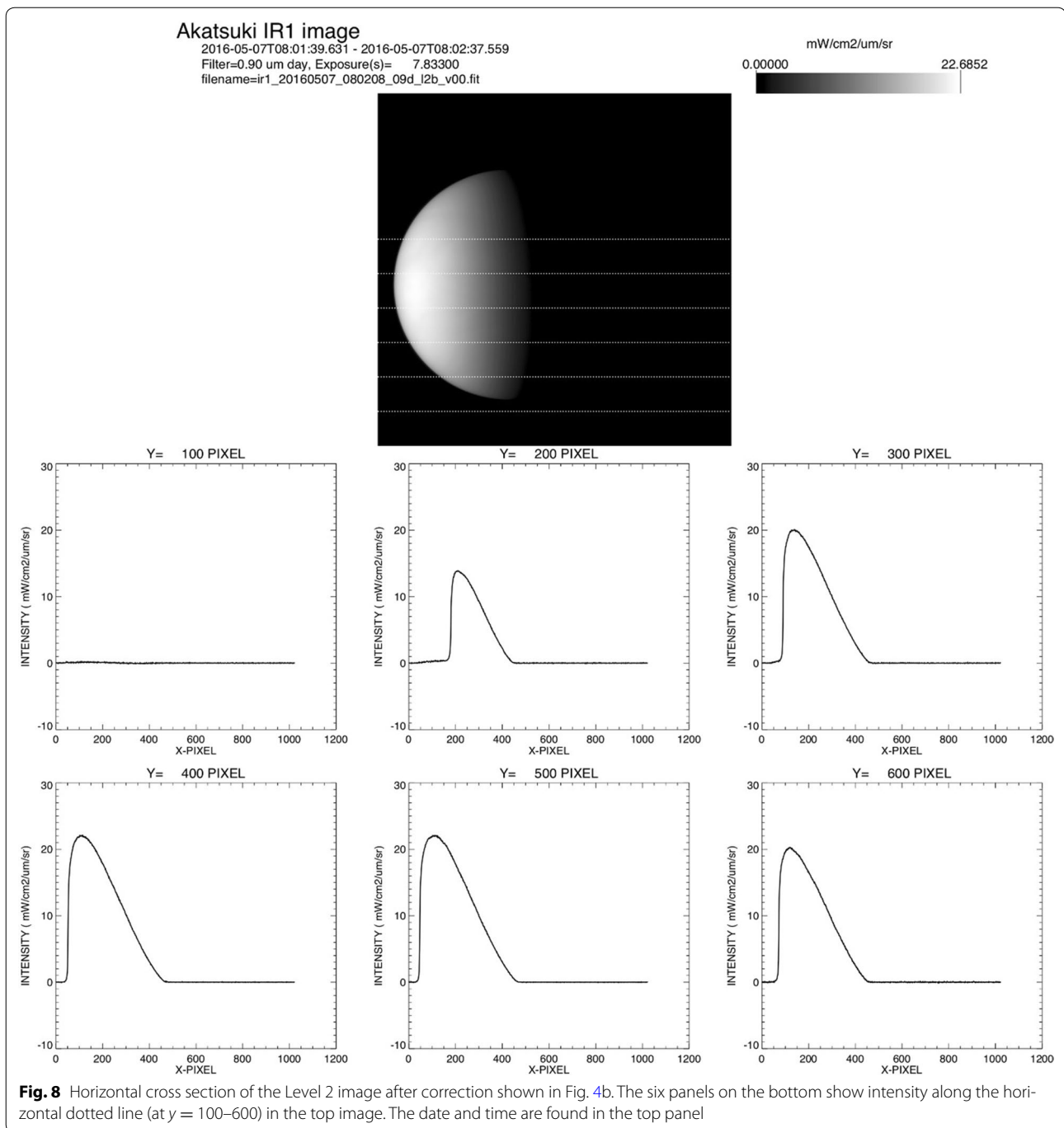
The observations of the stars with the 0.90-, 0.97- and 1.01-μm filters were performed three times on February 24, 2016, and five times on September 09, 2016. The sensitivity coefficients for the three nightside channels were estimated for each observation. The sensitivity coefficient for the 0.90-μm dayside channel was estimated by comparing the dayside and nightside transmissions. The estimated averaged sensitivity coefficients for the four

channels are shown in Table 4. The error was estimated as standard deviations of the sensitivity values.

The values in the table differ from those in Iwagami et al. (2011) because of the difference in the method; the latter method utilized laboratory measurements (without considering the smear correction), whereas the present one relies on the star measurements. Because of uncertainty in the smear correction for the laboratory

Iwagami *et al. Earth, Planets and Space* (2018) 70:6

Page 11 of 19

Fig. 9 Vertical cross section of the flat field. The top image is the flat field in relative unit. The nine panels on the bottom show intensity along the vertical dotted line (at *x* = 100–900) in the top image. Factor indicates relative brightness

Iwagami *et al. Earth, Planets and Space* (2018) 70:6

Page 12 of 19
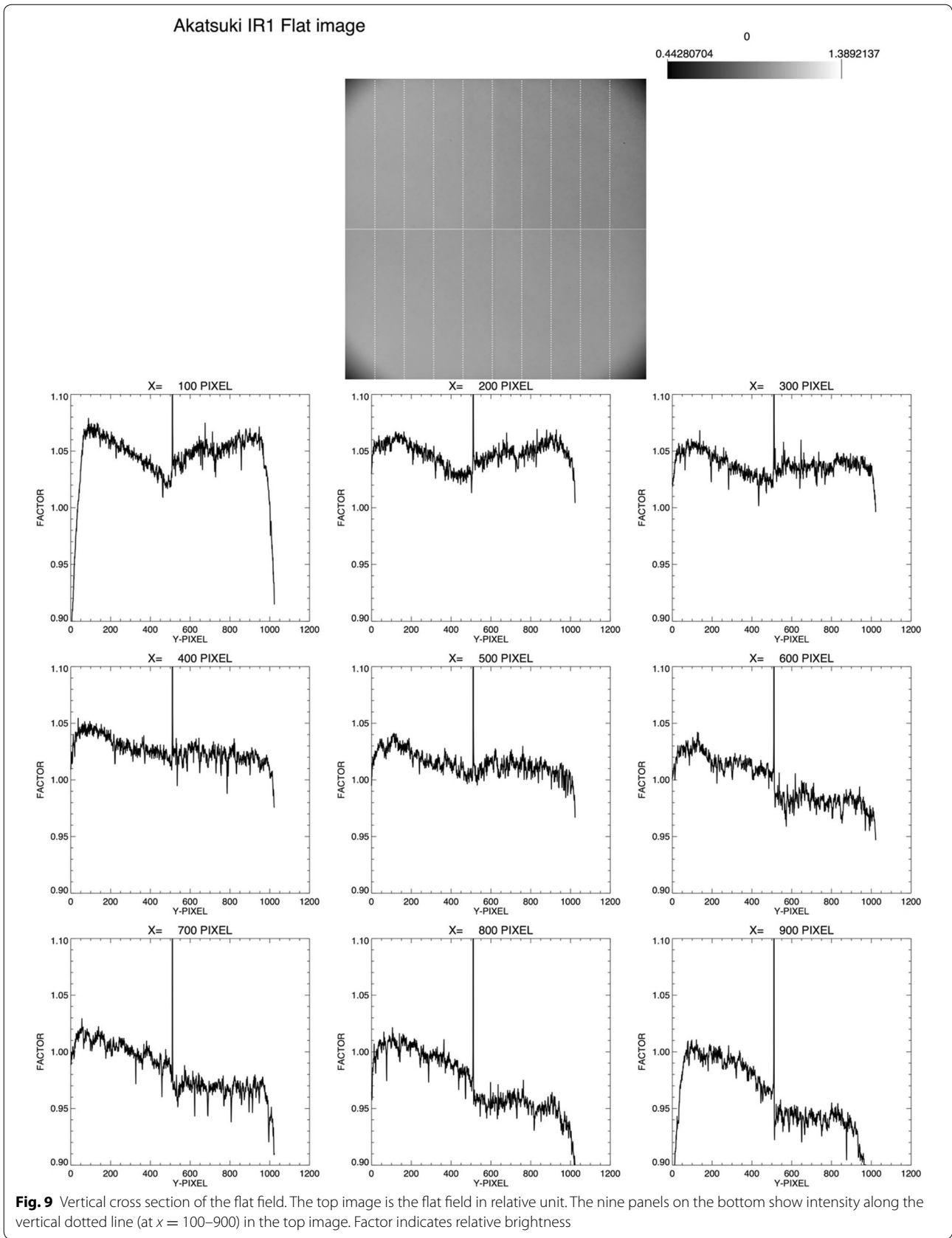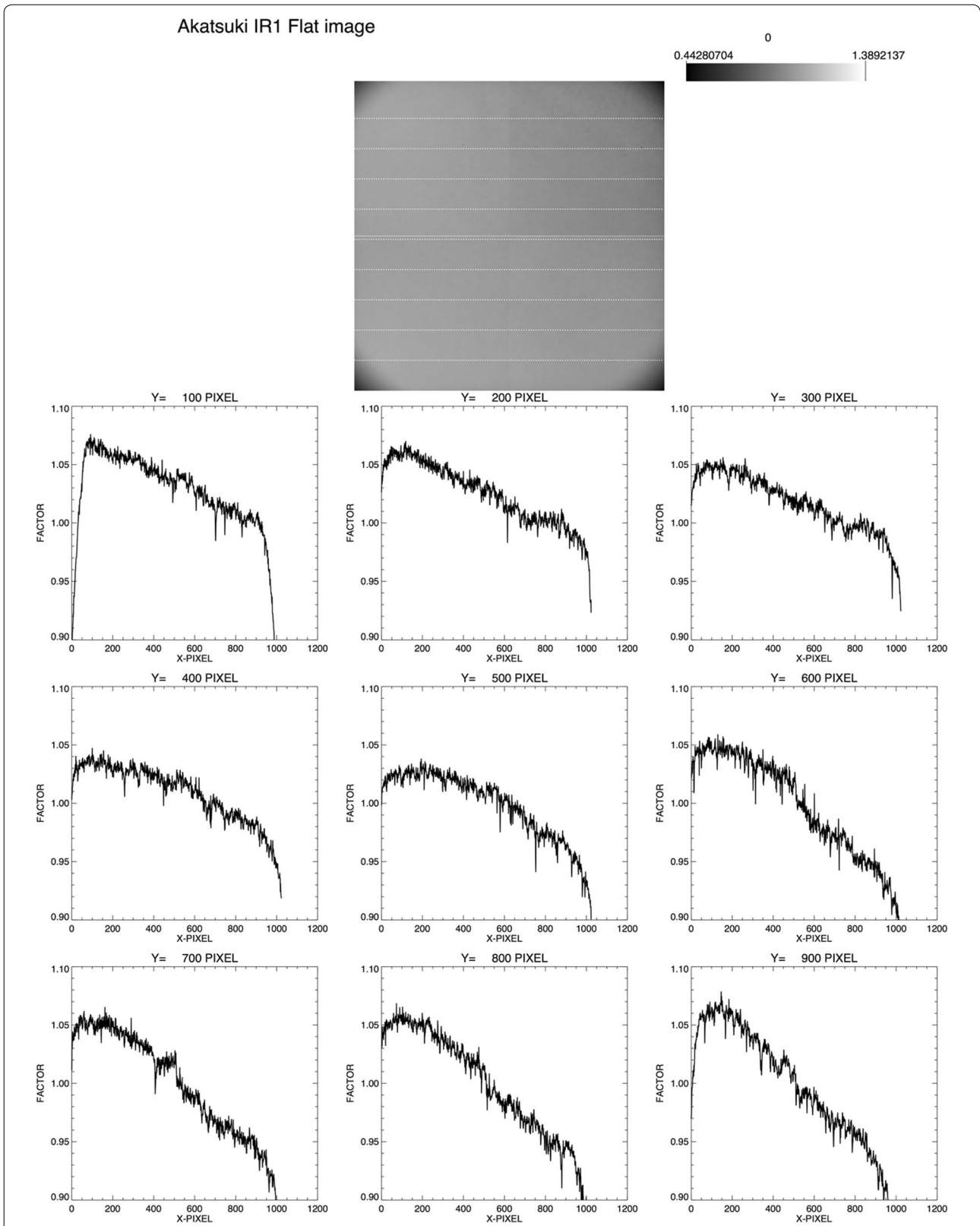
Fig. 10 Horizontal cross section of the flat field. The top image is the flat field in relative unit. The nine panels on the bottom show intensity along the horizontal dotted line (at $y = 100$–900) in the top image. Factor indicates relative brightness

Iwagami *et al. Earth, Planets and Space* (2018) 70:6

Page 13 of 19

measurements, we use the star measurements for the radiometric calibration. The radiometric calibration here may include error due to difference between the actual spectral shape and the black body due to absorption structure; this is not included in the error in Table 4.

Signal-to-noise ratio

The standard exposure is 7.8 s for the dayside to have usual output of around 3000 ADU (full well is 10,000 ADU), and the fluctuation in noise level for dayside image is 5 ADU which seems to be mostly due to read-out noise because the overall fluctuation in noise level for the nightside does not scale with exposure time. That is, it does not differ by a factor of four from that of day-side although the exposure duration differs by four times. The S/N (signal to noise) ratio of 600 is enough for the cloud tracking because the expected contrast is 3% as shown later. The standard exposure time for the nightside is 30.8 s. The fluctuation in thermal noise level seems to be much less than 5 ADU per 30.8 s when the detector is cooled to 260 K. The measured thermal noise level (not fluctuation) is around 40 ADU (2800 electrons)/30.8 s; this suggests a thermal noise fluctuation of 0.75 ADU ($= 40$ ADU/$2800^{1/2}$) which is much smaller than 5 ADU. The usual output of the 1.01-μm channel is around 500 ADU and satisfies a S/N ratio higher than 100, which is generally considered enough for a search of active volcanism (Iwagami et al. 2011); however, those of the 0.90- and 0.97-μm channels are around 150 ADU, which are less than expected, and may affect the quantification of H_2O values and the spatial resolution of H_2O abundance maps. The cause of this problem seems to be due to the readout noise which is higher than initially expected.

Figure 11 shows a Level 3 image (an image plotted on the Venus's latitude–longitude coordinates). The Level 2 to Level 3 conversion is to refine the latitude and longitude mapped to the planetary disk for each image as shown in Fig. 11 using a limb-fitting procedure (Ogohara et al. 2012).

Table 4 Sensitivity coefficients for the four channels of the 1-μm camera

Channel	Sensitivity coefficient*
0.90 μm (day)	61.7 ± 4.7
0.90 μm (night)	0.0756 ± 0.0058
0.97 μm	0.608 ± 0.070
1.01 μm	1.35 ± 0.91

The difference among nightside sensitivity coefficients as large as a factor of ten seems to come mostly from difference in quantum efficiency. Those wavelengths are near the edge of Si detector sensitivity at around 1.05 μm. The error due to difference between the actual spectral shape and the black body is not included here

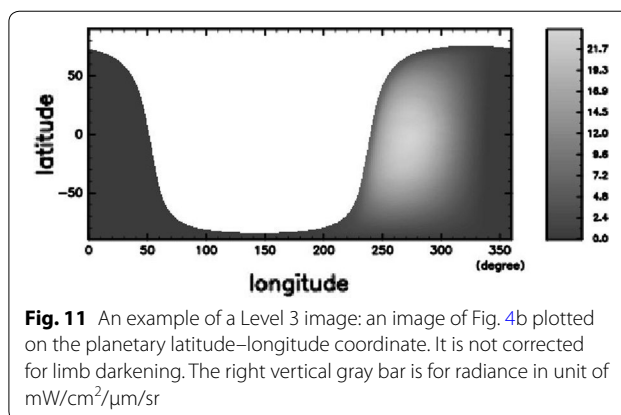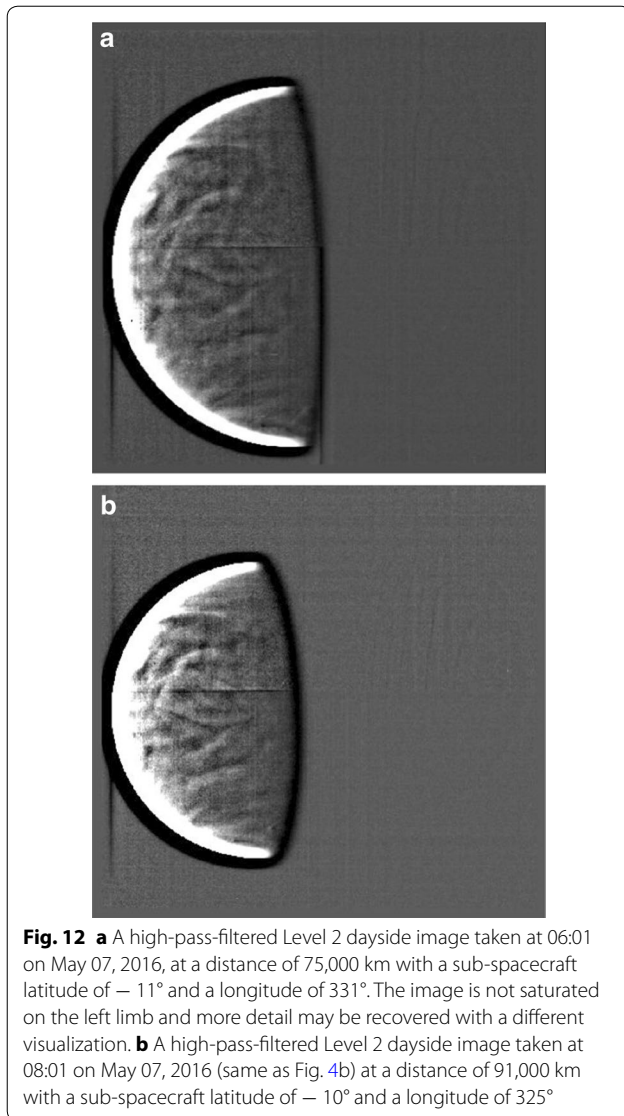*Unit: μW/cm^2/μm/sr/(ADU/s) where ADU = analogue to digital conversion unit

Fig. 11 An example of a Level 3 image: an image of Fig. 4b plotted on the planetary latitude–longitude coordinate. It is not corrected for limb darkening. The right vertical gray bar is for radiance in unit of mW/cm^2/μm/sr
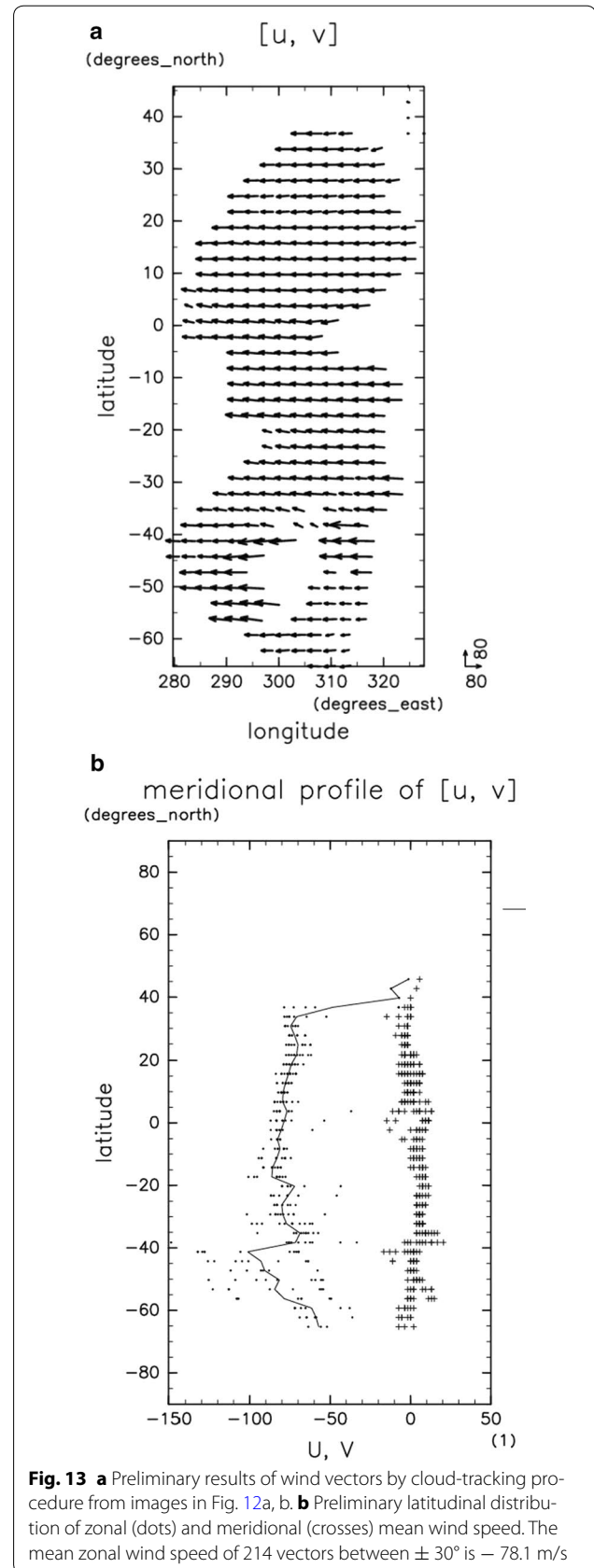
A dayside example on May 07, 2016

Examples of 0.90-μm dayside high-pass-filtered Level 2 images are shown in Fig. 12a, b. They were taken at 06:01 and 08:01 on May 07, 2016, with distances of 75,000 and 91,000 km, respectively. A high-pass filtering procedure is needed to enhance the contrast in the images (high-pass data) = (raw data)/(low-pass data), where the low-pass data are the local average of the raw data considering a weighting function. In the following, the weighting function used is a Gaussian with a FWHM (full width of half maximum) of 40 pixels. Almost no contrast is seen in the raw image shown in Fig. 4b as expected from the report of SSI/Galileo (Belton et al. 1991) where they found dayside contrast of only 3%. It may seem to be challenging to use such low contrast features for cloud tracking. However, after application of the high-pass filtering procedure, several structures may be recognized, as in Fig. 12a, b. It might be surprising to find similarity in those high-pass images in spite of 2-h separation. This is not an instrumental artifact, but is the result of the similarity between the orbital speed of Akatsuki's orbital motion (9° per 2 h) and that of the Super-Rotation (7.5° per 2 h) during this interval. The high-pass-filtered structures look stable on the disk. In the initial plan before the 2010 failure, such synchronization was planned considering a 30-h orbital period; however, the present actual orbital period is around 10 Earth-days. The representative height of the present 0.90-μm imaging is estimated to be around 51–55 km as will be discussed in a latter part of this section.

A cloud-tracking test was carried out by using the automated cloud-tracking method developed by Ikegawa and Horinouchi (2016) with an algorithm keeping deformation consistency developed by Horinouchi et al. (2017). Preliminary results are shown in Fig. 13a, b. The images used were taken on May 07, 2016, shown in Fig. 12a, b. It found similar results as Belton et al. (1991) based on SSI/Galileo 986-nm imaging and by Hueso et al. (2012)

Iwagami *et al. Earth, Planets and Space* (2018) 70:6

Page 14 of 19

Fig. 12 a A high-pass-filtered Level 2 dayside image taken at 06:01 on May 07, 2016, at a distance of 75,000 km with a sub-spacecraft latitude of − 11° and a longitude of 331°. The image is not saturated on the left limb and more detail may be recovered with a different visualization. **b** A high-pass-filtered Level 2 dayside image taken at 08:01 on May 07, 2016 (same as Fig. 4b) at a distance of 91,000 km with a sub-spacecraft latitude of − 10° and a longitude of 325°

based on VIRTIS 980-nm imaging. They show dominance of a uniform westward wind with an average speed of 65–75 m/s and slow meridional wind at low and mid-latitudes. More interesting is the possible absence of meridional wind. This fact is significant to the generation mechanism of the Super-Rotation, especially regarding the "Gierasch mechanism" (Gierasch 1975), which requires angular momentum pumping by the meridional circulation. Further discussion will appear in a separate paper.

The reason why the representative height of the 0.90-μm dayside image is located at the cloud bottom comes from the fact "the source of 0.90 μm dayside contrast is inhomogeneous cloud thickness" as discussed by Takagi and Iwagami (2011). They checked three candidates (cloud thickness, cloud height and temperature) as the

Fig. 13 a Preliminary results of wind vectors by cloud-tracking procedure from images in Fig. 12a, b. **b** Preliminary latitudinal distribution of zonal (dots) and meridional (crosses) mean wind speed. The mean zonal wind speed of 214 vectors between ± 30° is − 78.1 m/s

Iwagami *et al. Earth, Planets and Space* (2018) 70:6

Page 15 of 19

contrast source and performed simulations with radiative transfer calculation. They found that only inhomogeneous cloud thickness can be the source. This is due to the fact that the cloud particles show almost no absorption at 0.90 µm. However, the main source of such inhomogeneity seems to be due to inhomogeneity in the lower cloud, or in other words, the mode 3 particles. Descriptions of the modes of the Venus aerosols may be found in Knollenberg and Hunten (1980).

The representative height depends on the cloud model used. In the present paper, the center of mass of the population of the mode 3 particles was calculated by using an empirical cloud model of Takagi and Iwagami (2011) (in their Table 2 and Fig. 3). This cloud model is an average of cloud optical thickness measurements by six Venera and one Pioneer Venus descent probes modified to have nearly constant particle mixing ratios within each assumed layer (lower, middle and upper). Description of the layers may be found in James et al. (1997). The center of mass of the population of the mode 3 particles is found to be 51.3 km and that of all three modes is at 55.1 km. The most significant variation in the cloud thickness is expected to occur in the lower cloud layer (mostly with mode 3 particles); this is certainly seen as the largest spread of optical thickness measured by the descending probes in the lower cloud layer in Table 1 of Takagi and Iwagami (2011). The main information source for the images in Fig. 12a, b should locate at least between 51 and 55 km and probably is close to 51 km.

Dayside example related to the Bow event on December 07, 2015

Figure 14 shows an image of the 10-µm camera showing a bow-shaped structure with a latitudinal scale of almost 10,000 km (Fukuhara et al. 2017). This feature was seen for the first time on the day of successful Venus's orbit insertion on December 07, 2015; such a large latitudinal structure had not been previously seen and reported at infrared wavelengths. A similar but less clear structure was also seen in the UV image (Fukuhara et al. 2017). They explain it by vertical propagation of a gravity wave generated by surface topography because the Bow is fixed relative to the surface for several days. The longitude of the Bow is 85° which is close to the west edge of Aphrodite Terra. A similar scenario of gravity wave vertical propagation is discussed by Bertaux et al. (2016) and by Peralta et al. (2017) based on ground-based and Venus Express data.

It is interesting to investigate whether any signature corresponding to the Bow was also seen in the 0.90-µm image or not. However, at a glance, there appears nothing correlating to the Bow in the 0.90-µm image (Fig. 15a) even after the high-pass filtering procedure (Fig. 15b). It may be natural because the 0.90-µm radiance is insensitive to

temperature contrast as noted before (Takagi and Iwagami 2011), and also the representative heights seen are different from each other; that for 0.90 µm is at 51–55 km, and those for 10 µm and UV are probably at the cloud top of 65–72 km (Belton et al. 1991; Hueso et al. 2012; Fukuhara et al. 2017). Also the bright south polar region shown in Fig. 14 is not shown in Fig. 15a, b; this can be understood by the insensitivity of the 0.90-µm imaging to temperature change. Although any corresponding structure is not seen in those images, it is interesting to check whether any correlation is found in the wind field or not.

A cloud-tracking test was carried out using the images taken at 04:51 (Fig. 15a, b) and 08:31 (not shown here) on December 07, 2015. Preliminary results are shown in Fig. 16a, b. Similar results were found for the May 07, 2016, example; that is, in both examples, we see a "uniform zonal wind of around 75 m/s and slow meridional wind at low and middle latitudes." This similarity suggests that the data acquisition and the processing are stable and reliable. The Bow appeared at a longitude of 85° and latitudes between ± 30°; however, no signature corresponding to the Bow is found in the 0.90-µm wind field. Further discussion will be found in a separate paper.

Nightside examples

Figure 17a, b shows examples of observed and simulated 1.01-µm nightside images, respectively. In the lower left of Fig. 17a, Aphrodite Terra extending over the equatorial region is recognized as a dark area. Since Aphrodite Terra is higher than the surrounding lowlands by 4 km, temperature there is about 30 K lower making the thermal radiance almost a half of the surrounding lowlands. It is surprising to see such a topographic signature so clearly, though topographic features have already been observed by ground-based observations (e.g., Lecacheux et al. 1993). Also there are Venus Express observations of the surface with both VIRTIS (Mueller et al. 2008) and VMC (Basilevsky et al. 2012).

Figure 17b shows a simulated radiance of surface thermal emission based on the Magellan global topography data (Ford and Pettengill 1992). Vertical temperature profile of VIRA 1985 (Seiff et al. 1985) and uniform surface emissivity are assumed. Although a blurring effect due to scattering by cloud particles is taken into account with an averaging diameter of 100 km (Hashimoto and Imamura 2001), the attenuation by scattering of clouds is not calculated. Limb darkening observed in Fig. 17a is not reproduced in Fig. 17b.

Similarity between Fig. 17a, b clearly demonstrates that we sense the surface by using 1.01-µm window. Since the 1-µm region is located short-ward of the Planck function peak of the Venus surface emission at 4 µm (at 740 K), a small temperature difference results in a large radiance difference; in this case, 30 K difference in temperature
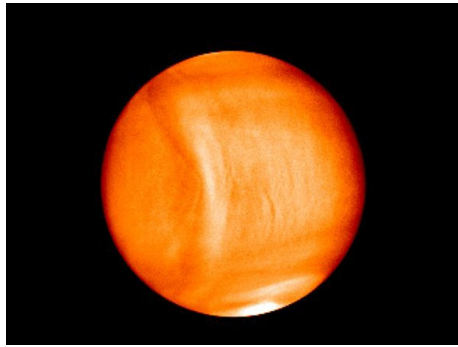
Iwagami *et al. Earth, Planets and Space* (2018) 70:6

Page 16 of 19

Fig. 14 A 10-μm image taken by LIR (Longwave InfraRed) camera at 05:26 on December 07, 2015, at a distance of 73,000 km with a sub-spacecraft latitude of − 7° and a longitude of 95°. The main Bow is seen near the center at around a longitude of 85° with a latitudinal extent of almost 10,000 km
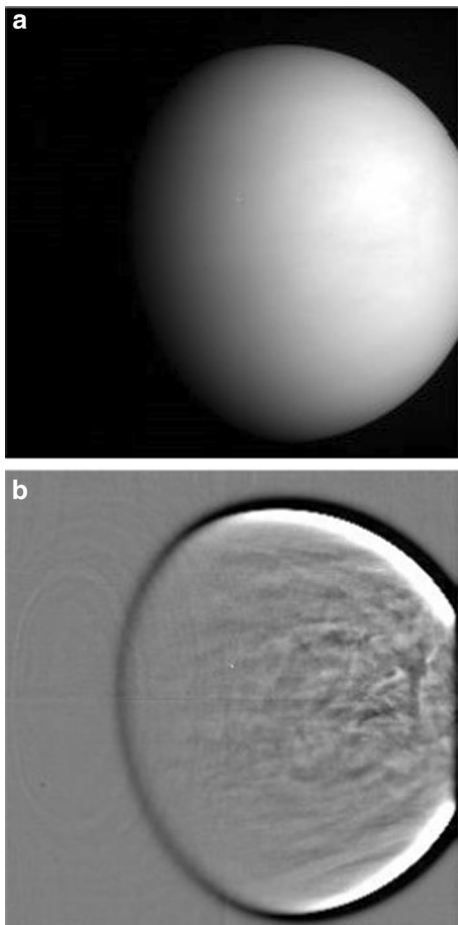

Fig. 15 a A 0.90-μm Level 2 dayside image at 04:51 on the same day as the Bow event in Fig. 14 at a distance of 68,000 km with a sub-spacecraft latitude of − 7° and longitude of 96°. **b** A high-pass-filtered image of Fig. 15a
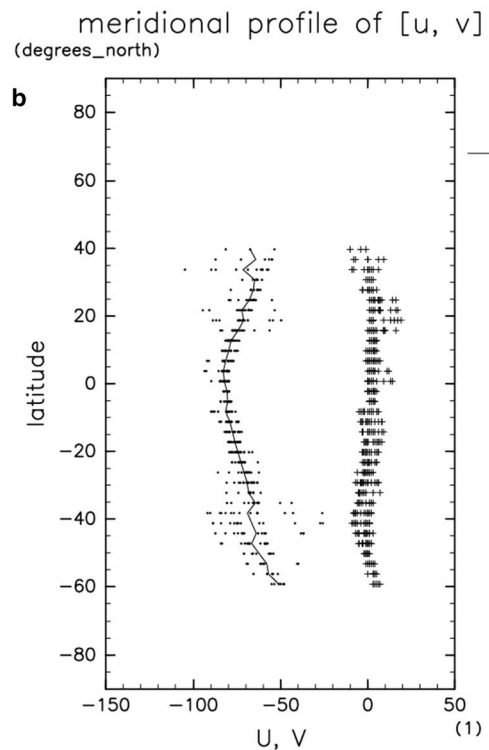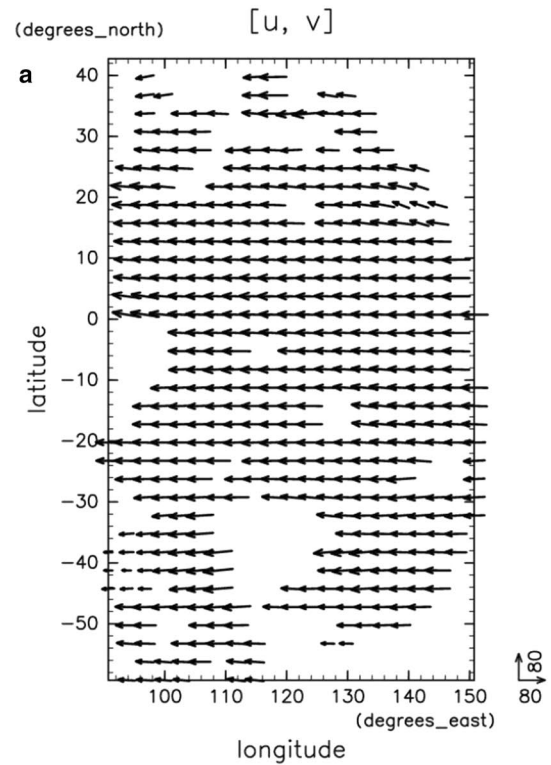
Fig. 16 a Preliminary results of wind vectors by cloud-tracking procedure from images taken at 04:51 (Fig. 15a) and 08:31 (not shown here) on December 07, 2015. **b** Preliminary latitudinal distribution of zonal (dots) and meridional (crosses) mean wind speed. The mean zonal wind speed of 340 vectors between ± 30° is − 76.4 m/s

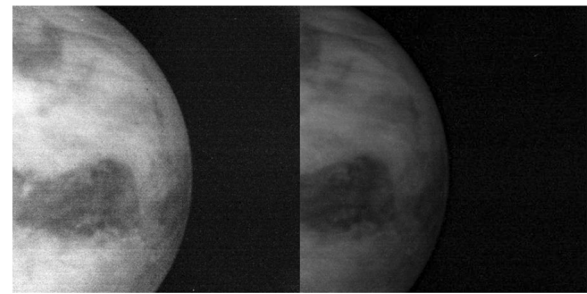Iwagami *et al. Earth, Planets and Space* (2018) 70:6

Page 17 of 19
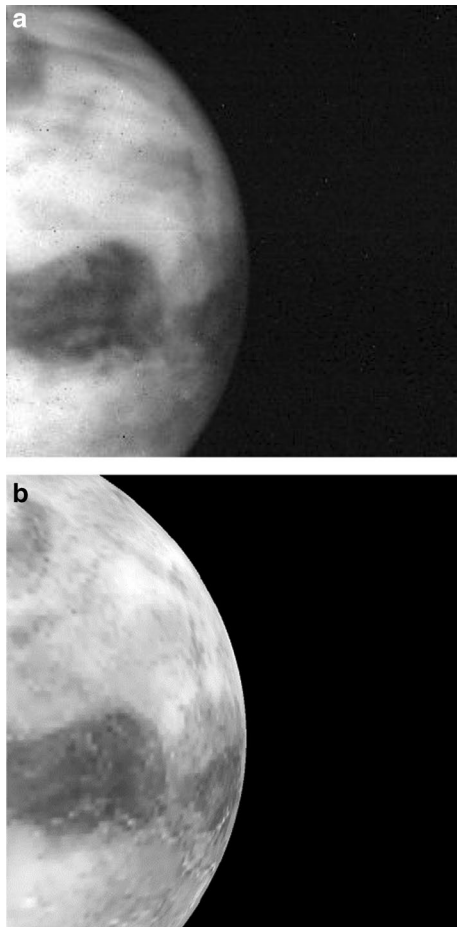
Fig. 17 a A 1.01-μm nightside Level 2 image at 00:38 on January 21, 2016, at a distance of 44,000 km with a sub-spacecraft latitude of + 3°, a longitude of 67° and a phase angle of 147°. **b** A preliminary 1.01-μm thermal radiance simulation intends to reproduce **a** based on the Magellan topographic information (Ford and Pettengill 1992) and VIRA 1985 (Seiff et al. 1985) temperature with uniform emissivity and 100-km smearing assumed without limb darkening

Fig. 18 (left): A 0.90-μm nightside Level 2 image at 00:44 on January 21, 2016, at a distance of 43,000 km with a sub-spacecraft latitude of + 3°, a longitude of 66° and a phase angle of 146°; (right): A 0.97-μm nightside Level 2 image at 00:37 on Jan. 21 2016, at a distance of 44,000 km with a sub-spacecraft latitude of + 3°, a longitude of 67° and a phase angle of 147°

the S/N ratio is as high as 100, the differential absorption pair of 0.97 and 1.01 μm can give a resolution of 5 ppmv (see Fig. 6 of Iwagami et al. 2011). The cause of this discrepancy may be due to underestimation of the read-out noise. Further discussion on the estimation of H_2O mixing ratio in the near-surface atmosphere will be presented in a separate paper.

Summary

High-quality 0.90-μm dayside images were recorded regularly. Two examples show results similar to those reported by Galileo and Venus Express 1-μm imaging (e.g., Peralta et al. 2007 for the Galileo data; Sanchez-Lavega et al. 2008; and Hueso et al. 2015 for the VIRTIS data), i.e., an almost uniform westward zonal wind and weak meridional wind at low and middle latitudes are observed. It shows enough possibility to access the final goal "the generation mechanism of the Super-Rotation."

The 1.01-μm nightside image shows topographic structures without large interference from cloud inhomogeneity and is suitable for the search of active volcanoes. The final goal of the nightside surface imaging is to investigate the origin and evolution of the planet Venus. The quantification of H_2O mixing ratio in the near-surface atmosphere may have less spatial resolution than originally planned, but is expected to provide usable data to understand the amount and distribution of H_2O near the surface.

causes 100% difference in radiance. Even though spatial inhomogeneity in cloud opacity affects the observation, we may be able to increase the accuracy of the measurement of the surface thermal emission by using cloud opacity estimated from 1.7- and/or 2.3-μm images taken by Akatsuki's 2-μm camera. If an active volcano is found and is monitored with repeat observations, further information inside the planet Venus may be obtained; such information on the interior of the planet may help to understand the origin and evolution of the planet.

The S/N ratio of 1.01-μm image is around 100 as expected, but those of 0.90 and 0.97 μm are around 30. Examples of 0.90- and 0.97-μm images taken nearly the same time as Fig. 17a are shown in Fig. 18. With the S/N ratio of 30, we can deduce the mixing ratio of H_2O in the near-surface atmosphere with a resolution of 15 ppmv; if

Iwagami *et al. Earth, Planets and Space* (2018) 70:6

Page 18 of 19

Author details
[1] Tokyo 156-0044, Japan. [2] Department of Geophysics, Tohoku University, Aramaki-aoba, Aoba-ku, Sendai 980-8578, Japan. [3] Department of Earth Sciences, Okayama University, Tsushima-Naka, Okayama 700-8530, Japan. [4] School of Commerce, Senshu University, 2-1-1 Higashimita, Tama-ku, Kawasaki, Kanagawa 214-8580, Japan. [5] Research and Information Center, Tokai University, 4-1-1 Kitakaname, Hiratsuka, Kanagawa 259-1292, Japan. [6] National Astronomical Observatory of Japan, 2-21-1 Osawa, Mitaka, Tokyo 181-8588, Japan. [7] Graduate School of Science, Kobe University, 7-1-48 Minatojima Minamimachi, Chuo-ku, Kobe, Hyogo 650-0047, Japan. [8] College of Science, Rikkyo University, 3-34-1 Nishi-Ikebukuro, Toshima-ku, Tokyo 171-8501, Japan. [9] Institute of Space and Astronautical Sciences, Japan Aerospace Exploration Agency, Sagamihara 252-5210, Japan. [10] Graduate School of Frontier Sciences, The University of Tokyo, 5-1-5 Kashiwanoha, Kashiwa, Chiba 277-8561, Japan. [11] School of Computer Science and Engineering, The University of Aizu, 90 Kami-Iawase, Tsuruga, Ikki-machi, Aizu-Wakamatsu, Fukushima 965-8580, Japan. [12] Planetary Exploration Research Center, Chiba Institute of Technology, 2-17-1 Tsudanuma, Narashino, Chiba 275-0016, Japan. [13] School of Engineering, University of Shiga Prefecture, 2500 Hassaka, Hikone, Shiga 522-8533, Japan. [14] Faculty of Science, Kyoto Sangyo University, Motoyama, Kamigamo, Kita-ku, Kyoto, Kyoto 603-8555, Japan. [15] Department of Information Engineering, National Institute of Technology, Matsue College, 14-4 Nishi-Ikuma, Matsue, Shimane 690-8518, Japan. [16] Department of Planetology/Center for Planetary Science, Kobe University, 7-1-48, Minamimachi, Minatojima, Chuo-ku, Kobe 650-0047, Japan. [17] Artificial Intelligence Research Center, National Institute of Advanced Industrial Science and Technology, 2-3-26 Aomi, Koto-ku, Tokyo 135-0064, Japan.

Competing interests
The authors declare that they have no competing interests.

Ethics approval and consent to participate
Not applicable.

Appendix A: Smear noise reduction

We estimated the non-uniform offset noise, smear in raw image, assuming that it is caused by weak photosensitivity of the vertical transfer device in the sensor unit and its level is constant in each vertical line (column). Its magnitude depends on the size and brightness of the planet over the detector but does not depend on the phase angle or filter being used. For example, the offset noise level in the i-th column in region A, $N_A(i)$, is calculated as follows,

$$N_A(i) = C_A \sum_{j=1}^{512} s_{in}(i,j),$$

where C_A is the smear noise coefficient for region A, and $s_{in}(i, j)$ is the input signal of the pixel (i, j). Note that the field of view is divided into four quadrants, A, B, C and D (see Fig. 2). The output signal $s_{out}(i, j)$ is expressed as $s_{in}(i, j) + N_A(i)$. Thus, the input signal (after subtraction of smear noise) is expressed as

$$s_{in}(i,j) = s_{out}(i,j) - C_A \left(\sum_{j=1}^{512} s_{out}(i,j) \right) \bigg/ (1 + 512 C_A).$$

The smear noise coefficients for the A–D regions are listed in Table 5. Note that the values for dayside observations with exposure time of 7.8 s are different from those for nightside observations with exposure time of 30.8 s. Note that we can make the dayside cloud distribution more clear, but until now, we cannot explain why smear noise level in the raw images is not uniform in the column as shown in Fig. 6 as non-flatness of the sky.

Table 5 Smear noise correction coefficients for quadrants A–D

	C_A	C_B	C_C	C_D
Dayside	0.0017274	0.0017215	0.0017316	0.0017838
Nightside	0.00066193	0.00066193	0.00071513	0.00071513

They are same for three nightside wavelengths because they have the same exposure time

Iwagami *et al. Earth, Planets and Space* (2018) 70:6

Page 19 of 19

Publisher's Note

References

Arney G, Meadows V, Crisp D, Schmidt SJ, Bailey J, Robinson T (2014) Spatially resolved mean of H_2O, HCl, CO, OCS, SO_2, cloud opacity, and acid concentration in the Venus near-infrared spectral windows. J Geophys Res 119:1860–1891. https://doi.org/10.1002/2014JE004662

Barstow JK, Tsang CCC, Wilson CF, Irwin PGJ, Taylor FW, McGouldrick K, Drossart P, Piccioni G, Tellmann S (2012) Models of the global cloud structure on Venus derived from Venus express observations. Icarus 217:542–560. https://doi.org/10.1016/j.icarus.2011.05.018

Basilevsky AT, Shalygin EV, Titov DV, Markiewicz WJ, Scholten F, Roatsch Th, Kreslavsky MA, Moroz LV, Ignatiev NI, Fiethe B, Osterloh B, Michalik H (2012) Geologic interpretation of the near-infrared images of the surface taken by the Venus monitoring camera, Venus express. Icarus 217:434–450

Belton MJS et al (1991) Images from Galileo of the Venus cloud deck. Science 253:1531–1536

Bertaux J-L et al (2016) Influence of Venus topography on the zonal wind and UV albedo at cloud top level: the role of stationary gravity waves. J Geophys Res. https://doi.org/10.1002/2015je004958

Bezard B, de Bergh C (2007) Composition of the atmosphere of Venus below the clouds. J Geophys Res 112:E04S07. https://doi.org/10.1029/2006JE002794

Bondarenko NV, Head JW, Ivanov MA (2010) Present-day volcanism on Venus: evidence from μ-wave radiometry. Geophys Res Lett 37:L32202

Carlson RW et al (1991) Galileo infrared imaging spectroscopy measurements at Venus. Science 253:1541–1548

Ford PG, Pettengill GH (1992) Venus topography and kilometer-scale slopes. J Geophys Res 97(E8):13103–13114

Fukuhara T et al (2017) Large stationary gravity wave in the atmosphere of Venus. Nat Geosci. https://doi.org/10.1038/ngeo2873

Gierasch PJ (1975) Meridional circulation and the maintenance of the Venus atmospheric rotation. J Atmos Sci 32:1038–1044

Hashimoto GL, Imamura T (2001) Elucidating the rate of volcanism on Venus: detection of lava eruptions using near-infrared observations. Icarus 154:239–243

Hashimoto GL, Roos-Serote M, Sugita S, Gilmore, Kamp LW, Carlson RW, Baines KH (2008) Felsic highland crust on Venus suggested by Galileo near-infrared mapping spectrometer data. J Geophys Res 113:E00B24. https://doi.org/10.1029/2008je003134

Horinouchi T, Murakami S, Kouyama T, Ogohara K, Yamazaki A, Yamada M, Watanabe S (2017) Image velocimetry for clouds with relaxation labeling based on deformation consistency. Meas Sci Technol 28:085301. https://doi.org/10.1088/1361-6501/aa695c

Hueso R, Peralta J, Sanchez-Lavega A (2012) Assessing the long-term variability of Venus winds at cloud level from VIRTIS-Venus express. Icarus 217:585–598

Hueso R, Peralta J, Garate-Lopez I, Bandos TV, Sánchez-Lavega A (2015) Six years of Venus winds at the upper cloud level from UV, visible and near infrared observations from VIRTIS on Venus express. Planet Space Sci 113–114:78–99. https://doi.org/10.1016/j.pss.2014.12.010

Ignatiev NI, Titov DV, Piccioni G, Drossart P, Markiewicz WJ, Cottini V, Roatsch T, Almeida M, Manoel N (2009) Altimetry of the Venus cloud tops from the Venus express observations. J Geophys Res 114:E00B43. https://doi.org/10.1029/2008je003320

Ikegawa S, Horinouchi T (2016) Improved automatic estimation of winds at the cloud top of Venus using superposition of cross-correlation surfaces. Icarus 271:98–119

Iwagami N, Ohtsuki S, Tokuda K, Ohira N, Kasaba Y, Imamura T, Sagawa H, Hashimoto GL, Takeuchi S, Ueno M, Okumura S (2008) Hemispheric distributions of HCl above and below the Venus' clouds by ground-based 1.7 μm spectroscopy. Planet Space Sci 56:1424–1434

Iwagami N, Yamaji T, Ohtsuki S, Hashimoto GL (2010) Hemispherical distribution of CO above the Venus' clouds by ground-based 2.3 μm spectroscopy. Icarus 207:558–563. https://doi.org/10.1016/j.icarus.2009.12.019

Iwagami N, Seiko Takagi S, Ohtsuki M, Ueno K, Uemizu T, Satoh T Sakanoi, Hashimoto GL (2011) Science requirements and description of the 1 μm camera onboard the Akatsuki Venus Orbiter. Earth Planets Space 63:487–492. https://doi.org/10.5047/eps.2011.03.007

James EP, Toon OB, Schubert G (1997) A numerical microphysical model of the condensational Venus cloud. Icarus 129:147–171

Kawabata K, Coffeen DL, Hansen JE, Lane WA, Sato M, Travis LD (1980) Cloud and haze properties from Pioneer Venus polarimetry. J Geophys Res 85:8129

Knollenberg RG, Hunten DM (1980) The microphysics of the clouds of the Pioneer Venus particle size spectrometer experiment. J Geophys Res 85:8039–8058

Lecacheux J, Drossart P, Laques P, Colas F (1993) Detection of the surface of Venus at 1.0 μm from ground-based observations. Planet Space Sci 41:543–549

Limaye SS, Suomi VE (1981) Cloud motions on Venus—Global structure and organization. J Atmos Sci 38:1220–1235

Marcq E, Bezard B, Drossart P, Piccioni G, Reess JM, Henry F (2008) A latitudinal survey of CO, OCS, H_2O, and SO_2 in the lower atmosphere of Venus: spectroscopic studies using VIRTIS-H. J Geophys Res 113:E00B07. https://doi.org/10.1029/2008je003074

Meadows VS, Crisp D (1996) Ground-based near IR observation of the Venus nightside: the thermal structure and water abundance near the surface. J Geophys Res 101:4595–4622

Mueller N, Helbert J, Hashimoto GL, Tsang CCC, Erard S, Piccioni G, Drossart P (2008) Venus surface thermal emission at 1 μm in VIRTIS imaging observations: evidence for variation of crust and mantle differentiation conditions. J Geophys Res 113:E00B17. https://doi.org/10.1029/2008je003118

Nakamura M et al (2011) Overview of Venus orbiter Akatsuki. Earth Planets Space 63:443–457. https://doi.org/10.5047/eps.2011.02.009

Nakamura M et al (2016) Akatsuki returns to Venus. Earth Planets Space 68:75. https://doi.org/10.1186/s40623-016-0457-6

Ogohara K, Kouyama T, Yamamoto H, Sato N, Takagi M, Imamura T (2012) Automated cloud tracking system for the Akatsuki Venus climate orbiter data. Icarus 217:661–668. https://doi.org/10.1016/j.icarus.2011.05.017

Peralta J, Hueso R, Sanchez-Lavega A (2007) A reanalysis of Venus winds at two cloud levels from Galileo SSI images. Icarus 190:469–477. https://doi.org/10.1016/j.icarus.2007.03.028

Peralta J, Hueso R, Sánchez-Lavega A, Lee YJ, García-Muñoz A, Kouyama T, Sagawa H, Sato TM, Piccioni G, Tellmann S, Imamura T, Satoh T (2017) Stationary waves and slowly moving features in the night upper clouds of Venus. Nat Astron 1:0187. https://doi.org/10.1038/s41550-017-0187

Sanchez-Lavega A, Hueso R, Piccioni G, Drossart P, Peralta J, Perez-Hoyos S, Wilson CF, Taylor FW, Baines KH, Luz D, Erard S, Lebonnois S (2008) Variable winds on Venus mapped in three dimensions. Geophys Res Lett 35:L13204. https://doi.org/10.1029/2008GL033817

SAO star catalogue, https://heasarc.gsfc.nasa.gov/W3Brouse/star-catalog/sao.html

Schubert G (1983) General circulation and the dynamical state of the Venus atmosphere. In: Venus, The University of Arizona Press, Tucson, pp 681–765

Seiff A, Shofield T, Kliore A, Taylor FW, Limaye SS, Revercomb HE, Sromovsky LA, Kerzanovich VV, Moroz VI, Marov M Ya (1985) Models of the structure of the atmosphere of Venus from the surface to 100 kilometers altitude. Adv Space Res 5(11):3–58

Smrekar SE, Stofan ER, Mueller N, Treiman A, Elkins-Tanton L, Helbert J, Piccioni G, Drossart P (2010) Recent hotspot volcanism on Venus from VIRTIS emission data. Science 328:605–608

Strand KA (ed) (1963) Basic astronomical data vol.3 stars and steller system. University of Chicago Press, Chicago, p 91

Takagi S, Iwagami N (2011) Contrast sources for the infrared images taken by the Venus mission Akatsuki. Earth Planets Space 63:435–442. https://doi.org/10.5047/eps.2011.01.007

Tsang CCC, Irwin PGJ, Wilson CF, Taylor FW, Lee C, de Kok R, Drossart P, Piccioni G, Bezard B, Calcutt S (2008) Tropospheric carbon monoxide concentrations and variability on Venus from Venus Express/VIRTIS-M observations. J Geophys Res 113:E00B08. https://doi.org/10.1029/2008JE003089